

# 1 Laboratory and theoretical modeling of air-sea momentum 2 transfer under severe wind conditions

3 Y. I. Troitskaya,<sup>1,2</sup> D. A. Sergeev,<sup>1,2</sup> A. A. Kandaurov,<sup>1,2</sup> G. A. Baidakov,<sup>1,2</sup> M. A. Vdovin,<sup>1,2</sup>  
4 and V. I. Kazakov<sup>1,2</sup>

5 Received 26 November 2011; revised 31 March 2012; accepted 8 May 2012; published XX Month 2012.

6 [1] The laboratory experiments on investigation of aerodynamic resistance of the waved  
7 water surface under severe wind conditions (up to  $U_{10} \approx 40 \text{ m s}^{-1}$ ) were carried out,  
8 complemented by measurements of the wind-wave spectra. The tendency to saturation of  
9 the surface drag was observed for wind speeds exceeding  $25 \text{ m s}^{-1}$ , accompanied by the  
10 saturation of wind-wave slopes. The effect of surface drag saturation can be explained  
11 quantitatively within the quasi-linear model of the air boundary layer above the waved  
12 water surface, when the contribution of the short-wave part of the wind-wave spectrum to  
13 aerodynamic resistance of the water surface is taken into account.

14 **Citation:** Troitskaya, Y. I., D. A. Sergeev, A. A. Kandaurov, G. A. Baidakov, M. A. Vdovin, and V. I. Kazakov (2012),  
15 Laboratory and theoretical modeling of air-sea momentum transfer under severe wind conditions, *J. Geophys. Res.*, 117,  
16 CXXXXX, doi:10.1029/2011JC007778.

## 17 1. Introduction

18 [2] One of the main characteristics appearing in the models  
19 of forecasting wind over the sea is air-sea momentum transfer  
20 determined by the parameters of the wind waves and quan-  
21 titatively parameterized by the sea surface drag coefficient  
22  $C_D$ . For definition  $C_D$ , we introduce the turbulent shear stress  
23 or turbulent momentum flux beyond the wave boundary layer

$$\tau_{turb}(z) = \rho_a u_*^2, \quad (1)$$

24 where  $\rho_a$  is the air density,  $u_*$  is the wind friction velocity. At  
25 the distance from the water surface much less compared to  
26 the Monin-Obukhov length determined by density stratifi-  
27 cation of atmospheric boundary layer, the wind is the turbu-  
28 lent boundary layer with the logarithmic mean velocity  
profile

$$U(z) = \frac{u_*}{\kappa} \ln \frac{z}{z_0}. \quad (2)$$

29 [3] Similar to the resistance law of the wall turbulent flow  
30 the sea surface drag coefficient is introduced as follows:

$$C_D = \frac{\tau_{turb}}{\rho_a U_{10}^2} = \frac{u_*^2}{U_{10}^2}, \quad (3)$$

where  $U_{10}$  is the wind velocity at a standard meteorological 31  
height  $H_{10} = 10 \text{ m}$ . Bulk formulas, which relate  $C_D$  to  $U_{10}$  are 32  
obtained either by compilation of empirical data [Garratt, 33  
1977; Large and Pond, 1981; Taylor and Yelland, 2001; 34  
Fairall et al., 2003] or by numerical modeling [see, e.g., 35  
Janssen, 1989, 1991; Makin et al., 1995; Hara and Belcher, 36  
2004]. Numerous field measurements give increasing depen- 37  
dencies of  $C_D$  on the wind speed, which is associated with the 38  
increase of wave heights with the wind. 39

[4] The aerodynamic drag coefficient of the sea surface is a 40  
critical parameter in the theory of tropical hurricanes: it is of 41  
special interest now in connection with the problem of 42  
explanation of the sea surface drag saturation at the wind 43  
speed exceeding  $30 \text{ m s}^{-1}$ . The idea of saturation (and even 44  
reduction) of the coefficient of aerodynamic resistance of the 45  
sea surface at hurricane wind speed was first suggested by 46  
Emanuel [1995] on the basis of theoretical analysis of sen- 47  
sitivity of maximum wind speed in a hurricane to the ratio of 48  
the enthalpy and momentum exchange coefficients. Both field 49  
[Powell et al., 2003; French et al., 2007; BAM, 2007; Jarosz 50  
et al., 2007] and laboratory [Donelan et al., 2004] experiments 51  
confirmed that despite the increase in surface wave heights 52  
at hurricane wind speed the sea surface drag coefficient is 53  
significantly reduced as compared with the parameterization 54  
obtained at moderate to strong wind conditions [Garratt, 55  
1977; Yelland and Taylor, 2001; Fairall et al., 2003]. 56

[5] Two groups of theoretical models were suggested to 57  
explain the effect of the sea surface drag reduction during 58  
hurricane winds. The first group of models [Kudryavtsev 59  
and Makin, 2007; Kukulka et al., 2007] explains the sea 60  
surface drag reduction by the peculiarities of the airflow over 61  
breaking waves, which determine the form drag of the sea 62  
surface. Similarly, in Donelan et al. [2004] the stabilization 63  
of the drag coefficient is qualitatively explained by a change 64  
in the shape of the surface elevation in dominant waves at 65

<sup>1</sup>Institute of Applied Physics, Russian Academy of Sciences, Nizhni  
Novgorod, Russia.

<sup>2</sup>Lobachevsky State University of Nizhni Novgorod, Nizhni Novgorod,  
Russia.

Corresponding author: Y. I. Troitskaya, Institute of Applied Physics,  
Russian Academy of Sciences, Ulyanova Str. 46, 603950 Nizhni Novgorod,  
Russia. (yuliya@hydro.appl.sci-nnov.ru)

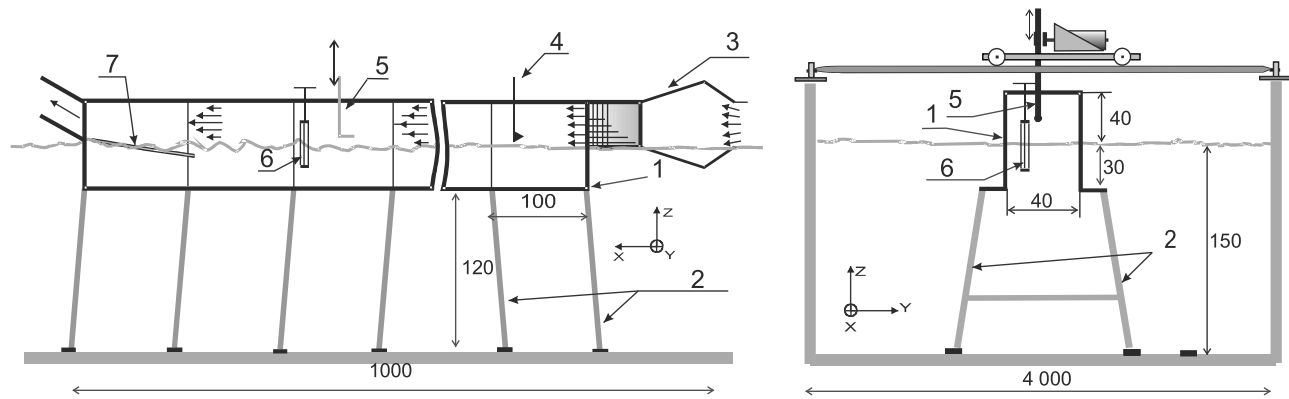


**Figure 1.** Sketch of experimental setup (1) straight part of flume, (2) vertical bearings, (3) expanding-narrowing section, (4) hot wire gauge, (5) Pitot tube on the scanning system, (6) three-channel string wave gauge, and (7) damping beach. All dimensions in cm.

66 wind velocities above  $35 \text{ m s}^{-1}$ , which is accompanied by  
 67 the occurrence of a steep leading front. In this case the  
 68 occurrence of flow separation from the crests of the waves is  
 69 assumed. This assumption is based on the laboratory  
 70 experiments by *Reul et al.* [1999], where airflow separation  
 71 at the crests of breaking waves was observed in the instant  
 72 velocity patterns by the Particle Image Velocimetry (PIV)  
 73 method. A close mechanism was suggested in the paper by  
 74 *Troitskaya and Rybushkina* [2008], where the sea surface  
 75 drag reduction at hurricane wind speed is explained by the  
 76 reduction of efficiency of wind-wave momentum exchange  
 77 at hurricane conditions due to sheltering without separation.  
 78 [6] Another approach, more appropriate for the conditions  
 79 of developed sea, exploits the effect of sea drops and sprays on  
 80 the wind-wave momentum exchange [*Andreas and Emanuel*,  
 81 2001; *Andreas*, 2004; *Makin*, 2005; *Kudryavtsev*, 2006;  
 82 *Kudryavtsev and Makin*, 2011]. *Andreas and Emanuel* [2001],  
 83 *Andreas* [2004], and *Kudryavtsev and Makin* [2011] estimated  
 84 the momentum exchange of sea drops and airflow, while  
 85 *Makin* [2005] and *Kudryavtsev* [2006] focused on the effect  
 86 of the sea drops on the stratification of the air-sea boundary  
 87 layer similar to the model of turbulent boundary layer with  
 88 the suspended particles by *Barenblatt and Golitsyn* [1974].  
 89 [7] In spite of the number of theoretical hypotheses, the  
 90 problem of explanation of the effect of surface drag reduction  
 91 at hurricane winds is not ultimately solved mostly due to the  
 92 lack of experimental data. The main aim of the present work  
 93 is a comprehensive study of the wind-wave interaction for the  
 94 hurricane wind conditions within the laboratory experiments  
 95 and theoretical modeling. The description of the experimental  
 96 setup for simultaneous measurements of airflow and surface  
 97 waves, peculiarities of data processing and experimental data  
 98 are presented in section 2 of the present work. In section 3 the  
 99 theoretical model used in this paper is described. In section 4  
 100 theoretical calculations of the surface drag coefficient are  
 101 compared with the experimental data described in section 2.

## 102 2. Laboratory Modeling of the Air-Sea 103 Interaction Under Hurricane Wind

104 [8] In this section we describe experimental setup, data  
 105 processing and the results of new laboratory experiments  
 106 devoted to the modeling of air-sea interaction at extremely  
 107 strong winds.

### 2.1. Experimental Setup and Instruments

[9] The experiments were performed in the wind-wave  
 flume located on top of the Large Thermostratified Tank of  
 the Institute of Applied Physics. The principal scheme of the  
 experimental setup is shown in Figure 1. The centrifugal fan  
 equipped with an electronic frequency converter to control  
 the discharge rate of the airflow produces the airflow in the  
 flume with the straight working part of 10 m. The operating  
 cross section of the airflow is  $0.40 \times 0.40 \text{ m}^2$ , whereas the  
 sidewalls are submerged at a depth of 0.30 m. During the  
 experiments axis velocity in the flume varied from 5 to  
 $25 \text{ m s}^{-1}$  (corresponds to  $U_{10}$  from  $7 \text{ m s}^{-1}$  to  $40 \text{ m s}^{-1}$ ).  
 The wave damping beach is placed at the airflow outlet at  
 the end of the flume.

[10] The aerodynamic resistance of the water surface was  
 measured by the profile method at a distance of 7 m from the  
 inlet. Wind velocity profiles were measured by the L-shaped  
 Pitot tube with the differential pressure transducer Baratron  
 MKS 226 A with the accuracy of 0.5% of full scale range,  
 i.e.,  $3 \text{ cm s}^{-1}$ . The lower level of scanning located at a  
 distance of 0.5 to 1 cm from the crests of the waves and  
 depended on the wind speed, while the upper layer was 38 cm  
 (in 2 cm below the upper lid of the channel). The scanning  
 method with the consecutive height increment of 3–5 mm  
 and accruing time of 2 min at each point was used. For each  
 fixed wind parameters, five profiles were measured for sub-  
 sequent averaging.

[11] Simultaneously with the airflow velocity measure-  
 ments, the wind-wave field parameters in the flume were  
 investigated by three wire gauges positioned in the corners  
 of an equal side triangle with 0.025 cm side, the data sam-  
 pling rate was 100 Hz (see Figure 1). Three dimensional  
 frequency-wave number spectra were retrieved from these  
 data by the algorithm similar to *Donelan et al.* [1996] based  
 on the window fast Fourier processing (see details below in  
 2.3). The experiment was accompanied by video filming of  
 the side view of the water surface.

### 2.2. Peculiarities of the Profile Method for Measuring the Surface Drag Coefficient in Aerodynamic Tunnels

[12] The classical profiling method of measuring the surface  
 drag coefficient is based on the property of the steady wall  
 turbulent boundary layer to conserve tangential turbulent

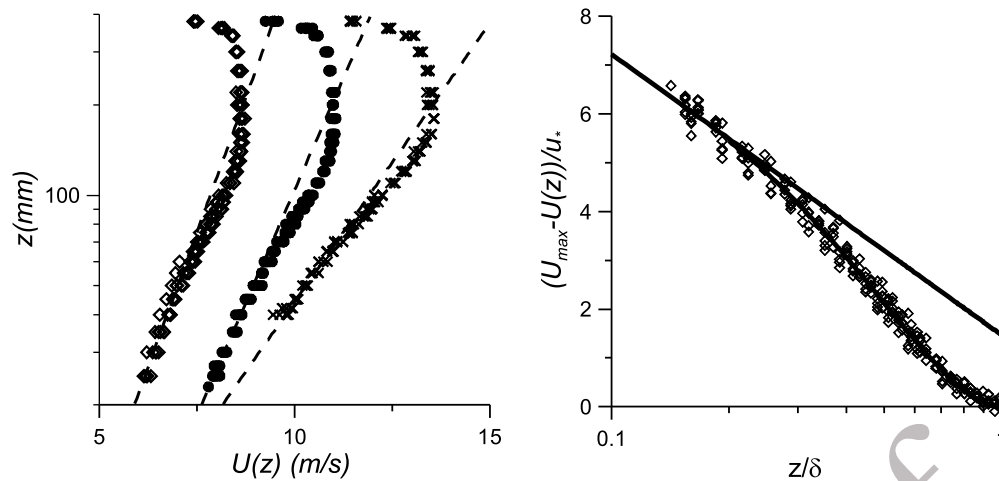


**Figure 2.** (left) Three examples of profiles in the aerodynamic flume over the waves for different inlet wind; dashed curves are logarithmic approximations in the layer of constant fluxes. I, the layer of constant fluxes; II, the “wake” part. (right) Airflow velocity profiles measured at different wind speeds over the waves in self-similar variables. The solid line is logarithmic approximation.

150 stress  $u_*^2$ , then the average flow velocity is logarithmic and  
 151 the wind friction velocity  $u_*$  can be easily determined from  
 152 (2), if the velocity profile is measured. However, developing  
 153 turbulent boundary layers are typical for the aerodynamic  
 154 tubes and wind flumes, then three sublayers at different dis-  
 155 tances from the water can be specified: the viscous sublayer,  
 156 the layer of constant fluxes and the “wake” part (see Figure 2,  
 157 left).

158 [13] The viscous sublayer, where viscous effects are  
 159 essential, exists over the hydrodynamically smooth surfaces  
 160 at the distances less than  $20 \div 30 \nu/u_*$  ( $\nu$  is the kinematic  
 161 viscosity), for moderate winds it is about 1 mm. The “wake”  
 162 part is the outer layer of the turbulent boundary layer, where  
 163 the boundary layer flow transits to the outer flow in the tube.  
 164 Its thickness  $\delta$  increases linearly from the inlet of the flume.  
 165 The layer of constant fluxes is extended from the upper  
 166 boundary of the viscous sublayer to approximately  $0.15\delta$ .

167 [14] Only in the layer of constant fluxes the flow velocity  
 168 profile is logarithmic and can be extrapolated to the standard  
 169 meteorological height  $H_{10}$ . Typically in aerodynamic tubes  
 170 and wind flumes the constant layer thickness is less than  
 171 0.10 m. Measuring wind velocity profiles at the distance less  
 172 than 10 cm from the wavy water surface at strong winds is a  
 173 difficult problem mainly due to the effect of sprays blown  
 174 from the wave crests. Fortunately, the parameters of the  
 175 layer of the constant fluxes can be retrieved from the mea-  
 176 surements in the “wake” part of the turbulent boundary  
 177 layer, because the velocity profile in the developing turbu-  
 178 lent boundary layer is described by the self-similar “law of  
 179 wake” [see *Hinze*, 1959]. The self-similar variables for the  
 180 velocity profile and vertical coordinates are  $z/\delta$  and  $(U_{\max} -$   
 181  $U(z))/u_*$ , where  $U_{\max}$  is the maximum velocity in the tur-  
 182 bulent boundary layer. The self-similar velocity profile can  
 183 be approximated by the following simple equations [see  
 184 *Hinze*, 1959]:

185 In the layer of constant fluxes

$$U_{\max} - U(z) = u_*(-2.5 \ln(z/\delta) + \alpha) \quad (4)$$

In the “wake” part

$$U_{\max} - U(z) = bu_*(1 - z/d)^2. \quad (5)$$

[15] Collapse of all the experimental points in one curve in  
 self-similar variables occurred in our experiments (see  
 Figure 2, right). The parameters in equations (4) and (5)  
 were obtained by the best fitting of the experimental data:  
 $\alpha = 1.5$ ,  $\beta = 8.5$ .

[16] The parameters of the logarithmic boundary layer can  
 be obtained from the measurements in the wake part of the  
 turbulent boundary layer, first, retrieving the parameters of  
 turbulent boundary layer ( $U_{\max}$  and  $\delta$ ) from best fit of the  
 experimental data by equation (5) and then calculating the  
 parameters of the logarithmic boundary layer by the fol-  
 lowing expressions:

$$U(z) = 2.5u_* \ln(z/z_0), \quad (6)$$

where

$$z_0 = \delta \exp(-\kappa U_{\max}/u_* + \alpha\kappa). \quad (7)$$

Expression for  $C_D$  via measured parameters  $u_*$ ,  $U_{\max}$  and  $\delta$   
 follows from equations (6) and (7):

$$C_D = \frac{\kappa^2}{(\kappa U_{\max}/u_* - \alpha\kappa + \ln(H_{10}/\delta))}. \quad (8)$$

[17] Wind velocity profiles were measured for 12 values  
 of the axis velocity from  $6 \text{ m s}^{-1}$  to  $24 \text{ m s}^{-1}$ .  $C_D$  and  $U_{10}$   
 were calculated by equations (8) and (4) respectively. The  
 obtained dependency of the surface drag coefficient on 10 m  
 wind speed is presented in Figure 3a together with the data  
 taken from the paper by *Donelan et al.* [2004]. The data  
 obtained at two different facilities are rather close to each  
 other both at the low and high wind speeds; the difference in  
 $C_D$  is less than 10%. The change in dependency of  $C_D$  on  
 $U_{10}$  is seen in both data sets at high winds, some differences,

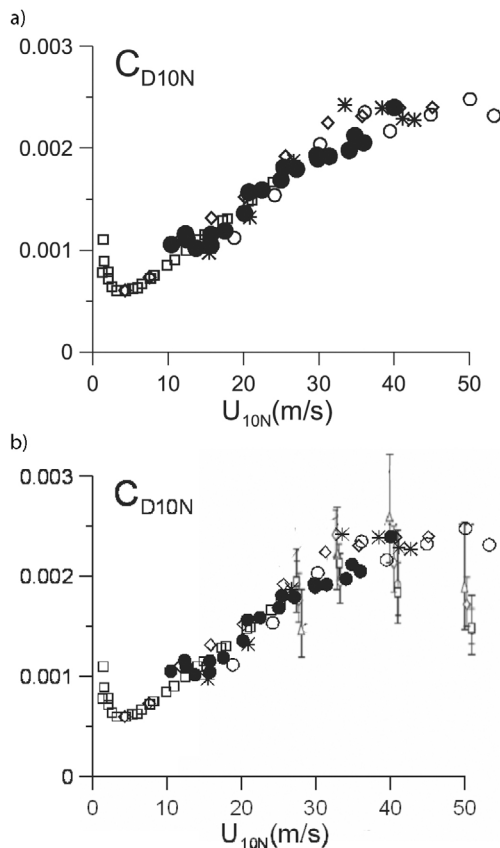


**Figure 3.** Surface drag coefficient. (a) Laboratory data: open symbols (squares, circles, diamonds, and asterisks) are taken from *Donelan et al.* [2004] and closed circles are measurements of the present work. (b) Compilation of the field measurements symbols with bars [*Powell et al.*, 2003] and laboratory data from Figure 3a. Reprinted/adapted by permission from Macmillan Publishers Ltd.

212 apparently due to differences in the details of data proces- 213  
sing. In *Donelan et al.* [2004] the leveling of  $C_D$  was 214  
observed for  $U_{10}$  exceeding 33 m/s. In these data a change 215  
in the angle of dependency of  $C_D$  on  $U_{10}$  occurs for  $U_{10}$  of 216  
about 25 m/s.

217 [18] In Figure 3b the laboratory data [*Donelan et al.*, 218  
2004] (and these data) are plotted together with the field 219  
data by *Powell et al.* [2003]. The quantities of  $C_D$  in labo- 220  
ratory and field conditions are close, but the decrease of  $C_D$  221  
for 10 m exceeding 35 m s<sup>-1</sup> reported in *Powell et al.* [2003] 222  
was not observed. The differences between laboratory and 223  
field data are expectable due to strong differences in fetch. 224  
Besides, as it was reported in *Young* [2003], at hurricane 225  
conditions the wavefield is dominated by the swell generated 226  
in the regions of high winds, which is not reproduced in 227  
laboratory conditions. Since the fetches in the laboratory 228  
facilities are much lower than in the field conditions, then 229  
the waves in the lab are shorter and steeper than in the sea, 230  
an enhanced aerodynamic resistance of the water surface can 231  
be expected. The additional reason suggested by *Donelan et* 232  
*al.* [2004] reads that in laboratory facility the wind-wave 233  
interaction is studied in stationary conditions of spatially 234  
developing turbulent boundary layer, while in the field

conditions, the wind in hurricane eye walls is strongly 235  
unsteady and represents an inhomogeneous flow. 236

### 2.3. Wavefield at Strong Winds in Laboratory Conditions

[19] Aerodynamic roughness of the sea surface is condi- 239  
tioned to waves at the water surface including strong wind 240  
conditions. According to *Powell* [2007], the surface drag 241  
depends significantly on the sector of the tropical cyclone, 242  
where it is measured. The sea surface drag is strongly 243  
enhanced in the left front sector of the tropical cyclone in 244  
comparison with the right and rare sector. *Powell* [2007] 245  
pointed out that although the data are insufficient for final 246  
conclusions, it seems that the aerodynamic drag depends on 247  
the wavefield, which is significantly different in different 248  
sectors of the tropical cyclone. In this paper the correlation 249  
of the wavefield parameters and aerodynamic surface resis- 250  
tance was investigated to elucidate the origin of the satur- 251  
ation of  $C_D$  with the wind growth. 252

[20] The wind-wave field parameters in the flume were 253  
measured by three wire gauges positioned in the corners of 254  
an equal side triangle with 2.5 cm side; the data sampling 255  
rate was 100 Hz. Three dimensional frequency-wave num- 256  
ber spectra were retrieved from these data by the algorithm 257  
similar to the wavelet directional method (WDM) suggested 258  
by *Donelan et al.* [1996]. Time series of water elevation 259  
from the wave staffs were processed by the window FFT 260  
with the window width  $2^N$  ( $N$  is an integer) without over- 261  
lapping. The complex amplitudes of harmonics at each fre- 262  
quency  $\omega$ :  $A_\omega(x_n, y_n) \exp(i\varphi_\omega(x_n, y_n))$  were calculated, here 263  
 $n = 1, 2, 3$  is the number of the wave staff. Suppose, that the 264  
wavefield is a superposition of harmonic waves with the 265  
wave numbers  $\vec{k} = (k_x, k_y)$  266

$$A_\omega(x_n, y_n) \exp(i\varphi_\omega(x_n, y_n)) = \sum_{x,y} A_{x,y}(\omega) \exp(i(k_x x_n + k_y y_n)), \quad (9)$$

and one harmonic wave dominates in each interrogation 267  
window (the applicability of this supposition is verified 268  
below), then 269

$$\varphi_\omega(x_n, y_n) = k_x x_n + k_y y_n. \quad (10)$$

[21] And the wave number components can be calculated 270  
by the phase difference at different wave staffs 271

$$\Delta\varphi_{n,m} = \varphi_\omega(x_n, y_n) - \varphi_\omega(x_m, y_m). \quad (11)$$

[22] In these experiments three wave staffs were used, 272  
then

$$\begin{aligned} k_x &= (\Delta\varphi_{1,2}\Delta y_{1,3} - \Delta\varphi_{1,3}\Delta y_{1,2})/\Delta, \\ k_y &= (\Delta\varphi_{1,3}\Delta x_{1,2} - \Delta\varphi_{1,2}\Delta x_{1,3})/\Delta, \\ \Delta &= \Delta x_{1,2}\Delta y_{1,3} - \Delta x_{1,3}\Delta y_{1,2}. \end{aligned} \quad (12)$$

[23] To obtain the directional spectra the Cartesian coor- 273  
dinates  $(k_x, k_y)$  were transformed to the polar coordinates 274  
 $(k, \theta)$  by  $k_x = k \cos \theta$ ,  $k_y = k \sin \theta$ . 275

[24] Then 3-D frequency-wave number spectrum  $S(\omega, k, \theta)$  276  
was obtained similar to *Donelan et al.* [1996] by binning the 277

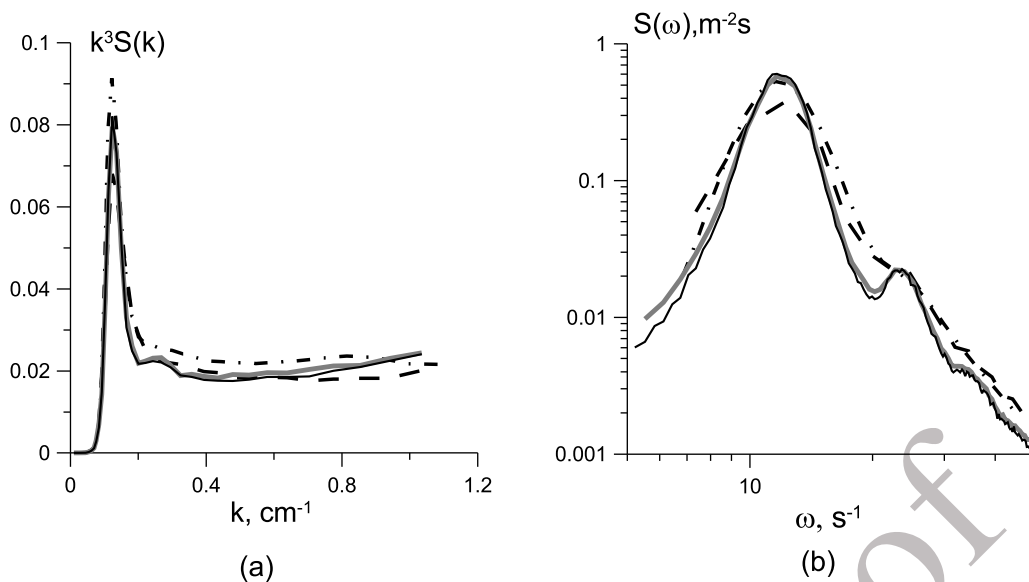


**Figure 4.** (a) Omnidirectional wave number saturation spectra and (b) frequency spectra. Obtained by the window FFT for the windows 1024 points (solid black line), 512 points (solid gray line), 128 points (dashed line), and by WDM (dash-dotted line).

278 amplitudes squared into calculated bins in  $k$  and  $\theta$ . Integrat-  
279 ing  $S(\omega, k, \theta)$  over wave number or frequency yields fre-  
280 quency  $S(\omega, \theta)$  or wave number  $S(k, \theta)$  directional spectra  
281 respectively. Integrating over  $\theta$  gives the omnidirectional  
282 frequency spectra and the wave number spectra correspond-  
283 ingly. The upper limit of the wave number spectrum is pre-  
284 scribed by the distance between the wave staffs  $d$ ,  $k_u = \pi/d$ ,  
285 in our experiments  $k_u = 1.25 \text{ cm}^{-1}$ .

286 [25] The developed algorithm is based on the supposition  
287 that the dominating wavefield within the interrogation win-  
288 dow at a given frequency  $\omega$  is a harmonic wave, which is  
289 correct for a rather short time interval due to groupiness of the  
290 surface wavefield. To check the applicability of this suppo-  
291 sition we investigated the dependence of the spectra on the  
292 width of the interrogation window. In Figure 4a an example  
293 of the omnidirectional wave number saturation spectra  
294 retrieved from the records of 3 waves staffs are shown for  
295 the windows of 128 points (1.28 s), 512 points (5.12 s) and  
296 1024 points (10.24 s) widths, the total length of the record  
297 was about 800,000 points (8000 s). It is clear that the  
298 tenfold variation of the window width only slightly affects  
299 the wave number spectra. Besides, in Figure 4a the omni-  
300 directional wave number saturation spectra retrieved from  
301 the same record by WDM algorithm [Donelan et al., 1996]  
302 is shown. The difference between the spectra given by both  
303 algorithms is less than 15%. The advantage of high spectral  
304 resolution of the window FFT against the wavelet trans-  
305 formation illustrates Figure 4b, where frequency elevation  
306 spectra are plotted: the use of the 1024 point and 512 point  
307 windows of width even enabled us to resolve secondary  
308 peaks in frequency and wave number spectra, while the  
309 spectra obtained for 1024 point and 512 point windows are  
310 hardly discernable. Concerning these estimations, we used  
311 the algorithm based on the window FFT with the window  
312 width of 512 points (or 5.12 s).

[26] The wind-wave saturation spectra at different 10 m 313  
wind speeds  $U_{10}$  are plotted in Figure 5a. The presence of a 314  
sharp peak downshifting with the increasing wind speed and a 315  
long plato is typical for the measured spectra. The dependen- 316  
cies of main integral parameters of surface waves on the wind 317  
speed were investigated. In Figure 5 the significant wave 318  
height ( $SWH$ ) (Figure 5b), peak wave number  $k_p$  (Figure 5c) 319  
and peak frequency  $\omega_p$  (Figure 5d) are presented via 10 m 320  
wind speed. Curves are power best fitting of experimental 321  
points, which gives  $SWH \sim U_{10}^{1.5}$ ,  $k_p \sim U_{10}^{-1.45}$  and 322  
 $\omega_p \sim U_{10}^{0.72}$ . As a result, the slope of the spectral peak pro- 323  
portional to the product of the significant wave height and the 324  
peak wave number ( $S_p = k_p SWH/4$ ) only slightly depends on 325  
the wind speed (see Figure 6, open circles), that probably 326  
corresponds to the regime of the saturation of the peak waves 327  
similar to reported by Donelan et al. [2004]. The dependence 328  
of the peak frequency on the peak wave number was compared 329  
with the linear dispersion relation for free surface waves  $\omega =$  330  
 $\sqrt{gk}$  in Figure 5e. It is visible that the experimental frequencies 331  
of the waves are about 10% above those given by the linear 332  
dispersion relation. It can be explained by the cumulative 333  
effect of nonlinearity of the waves, wind drift flow and the 334  
wind. 335

[27] In Figure 6 we present the dependencies of the mean 336  
square slope on the wind velocity. The open circles show the 337  
mean square slope of the peak wave  $S_p$ . Other symbols 338  
present the mean square slope of the wavefield calculated 339  
according to the definition 340

$$Slope = \int_{k_{min}}^{k_{max}} k^2 S(k) dk, \quad (13)$$

where  $S(k)$  is the omnidirectional elevation spectrum. 341

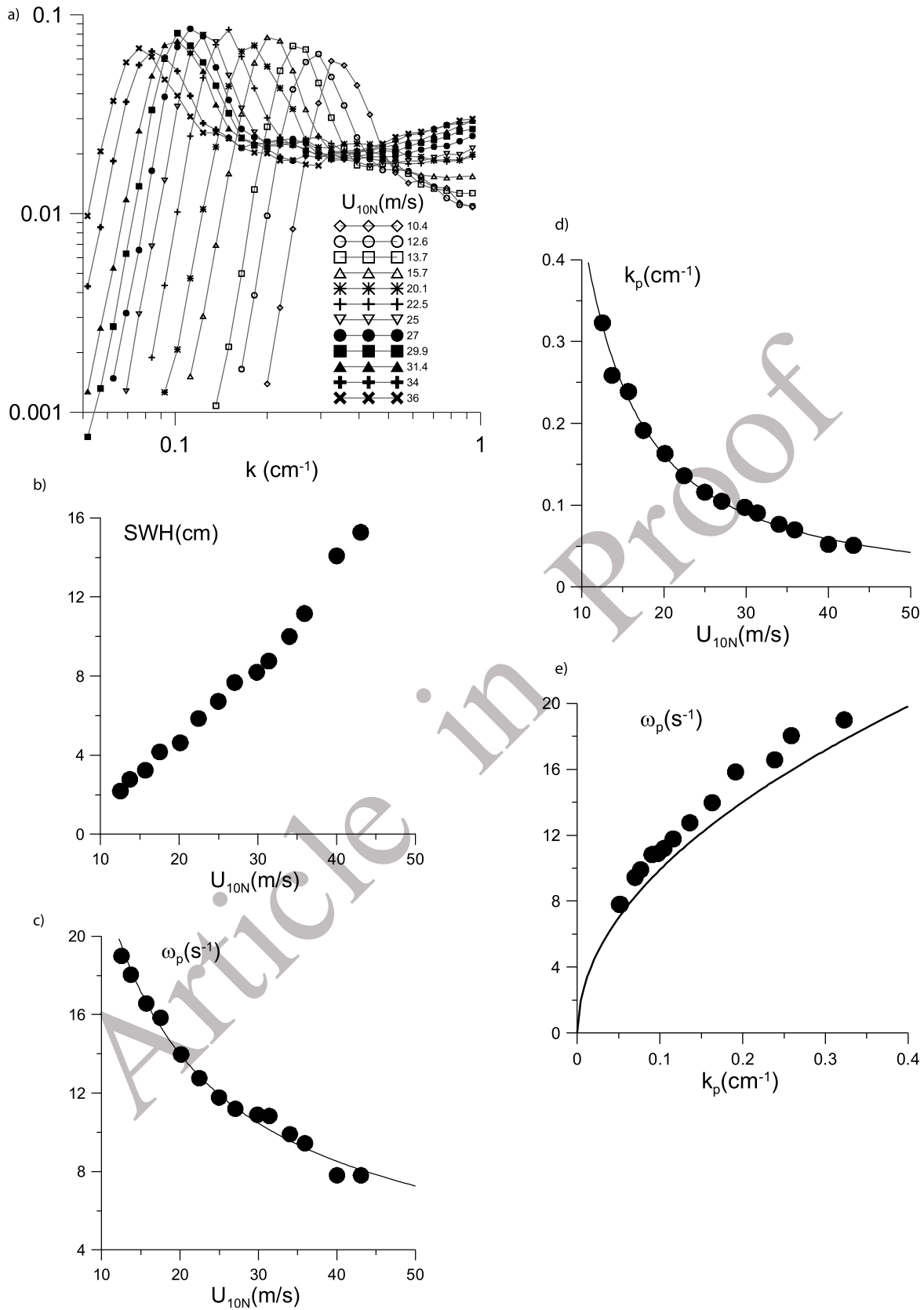


**Figure 5.** (a) Saturation wave number spectrum of the waves for a definite fetch (7 m) and different wind speeds  $U_{10}$ , (b) the dependence of the significant wave height on  $U_{10}$ , (c) the dependence of peak wave number on  $U_{10}$ , (d) the dependence of the peak wave frequency, and (e) the comparison of the dependence of the peak frequency on the peak wave number with the linear dispersion relation for free surface waves.

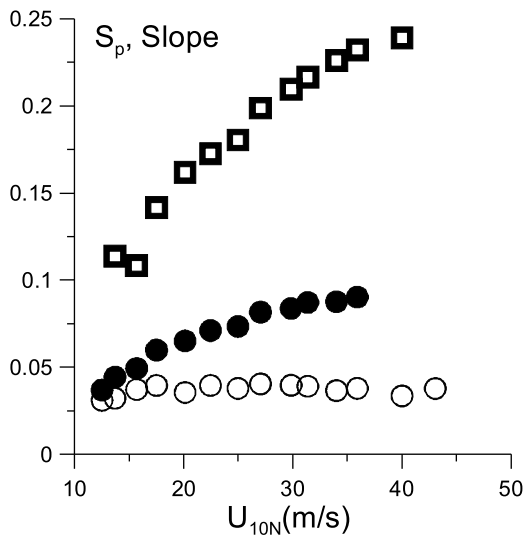


**Figure 6.** Dependences of the mean square slope on the wind velocity defined as  $(a_p k_p)/2$  (open circles). The calculated accordingly integral (13) for  $k_{\max} = k_u$  (solid circles) and  $k_{\max} = 20 \text{ m}^{-1}$  (open squares).

342 [28] Here the upper limit  $k_{\min} = 0.01 \text{ cm}^{-1}$  was selected  
 343 below the lowest wave number observed in the experiments.  
 344 It is well known, that the integral (13) strongly depends on  
 345 the upper limit  $k_{\max}$ . Measurements with the array of 3 wave  
 346 staffs provide  $k_{\max} = k_u = 1.25 \text{ cm}^{-1}$ . The dependence  
 347  $Slope(U_{10})$  for this upper limit is shown in Figure 6 by  
 348 solid circles.

349 [29] To take into account the short wave ripples both  
 350 generated near the crests of the waves due to wave breaking  
 351 and excited by the wind, we continued the spectrum for  $k >$   
 352  $k_{\max}$  by the model based on the ideas suggested by  
 353 *Elfouhaily et al.* [1997]. The model omnidirectional spec-  
 354 trum  $S(k)$  at  $k > k_u$  is considered as a sum of low-frequency  
 355  $S_l(k)$  and high-frequency  $S_h(k)$  terms

$$S(k) = S_l(k) + S_h(k). \quad (14)$$

356 [30] The expression suggested by *Elfouhaily et al.* [1997]  
 357 was taken to model  $S_h(k)$ :

$$S_h(k) = \frac{10^{-2}}{2} \left( 1 + a \ln \frac{u_*}{c_m} \right) \frac{c_m}{c} e^{-\frac{1}{4} \left( \frac{k}{k_m} - 1 \right)^2},$$

$$a = \begin{cases} 1 & \text{for } u_* < 23 \text{ cm/s} \\ 3 & \text{for } u_* > 23 \text{ cm/s} \end{cases}. \quad (15)$$

358 Here  $c_m = 23 \text{ cm s}^{-1}$ ,  $k_m = c_m 2/g$ .

359 [31] The low-frequency part  $S_l(k)$  was continued for  $k > k_u$   
 360 assuming the constant saturation spectrum, then

$$S_l(k) = \frac{\alpha}{k^3}.$$

[32] The constant  $\alpha$  was selected from the condition, that  
 at  $k = k_u$  the model spectrum coincides with the measured  
 one  $S(k_u)$ , then the omnidirectional spectrum at  $k > k_u$

$$S(k) = (S_l(k_u) - S_h(k_u)) \left( \frac{k_u}{k} \right)^3 + S_h(k). \quad (16)$$

[33] The angular dependence of the spectrum at  $k > k_u$  was  
 selected the same as it was measured at

$$k = k_u : f(\theta) = S(k_u, \theta) / S(k_u).$$

[34] The mean square slope calculated for the composite  
 spectrum with the upper limit  $k_{\max} = 20 \text{ cm}^{-1}$  is shown by  
 squares in Figure 6 as a function of  $U_{10}$ . Figure 6 clearly  
 shows, that for both values of the upper limit  $k_{\max}$  in the  
 integral (13) the mean square slope tends to saturation when  
 $U_{10} > 25 \text{ m s}^{-1}$ . The comparison with the Figure 5a shows  
 that the saturation spectrum as a whole demonstrates the  
 tendency to saturation for  $U_{10} > 25 \text{ m s}^{-1}$ . It means that at  
 the wind speed about  $25 \text{ m s}^{-1}$  the regime changing of the  
 wavefield occurs. The comparison of the dependencies of  
 the wave slope on the wind speed in Figure 6 and the drag  
 coefficient dependency in Figure 3 shows, that the change in  
 the wavefield regime correlated with the tendency to satu-  
 ration of the surface drag dependence on the wind speed and  
 Figure 7 clearly shows linear dependence between the  
 surface drag coefficient and the mean square slope for both  
 values of the upper limit  $k_{\max}$  in the integral (13).

[35] The photos of the side views of the water surface  
 (Figure 8) elucidate a possible origin of the change in the  
 regime of the wavefield at 10 m wind speeds exceeding  
 $25 \text{ m s}^{-1}$ . Starting from this threshold, the wave breaking is  
 intensified, because the crests of the waves are blown away  
 by the strong tangential wind stress. It is accompanied with  
 sprays, drops and bubbles near the wave crests, visible at  
 the photos. Blowing away the crests of waves which steep-  
 ness exceeds, a definite threshold leads to the effective

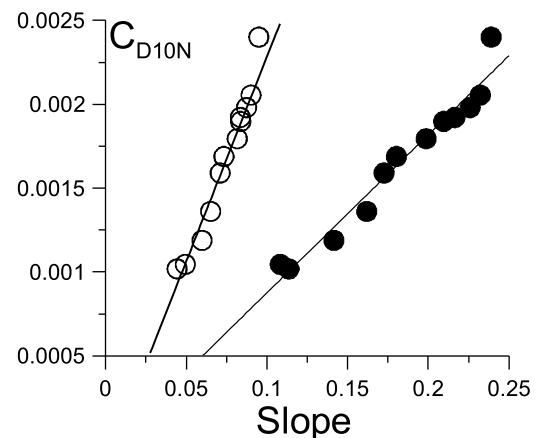


**Figure 7.**  $C_D$  against mean square slope diagram. Solid symbols are for  $k_{\max} = 20 \text{ m}^{-1}$  and open symbols are for  $k_{\max} = k_u$ .

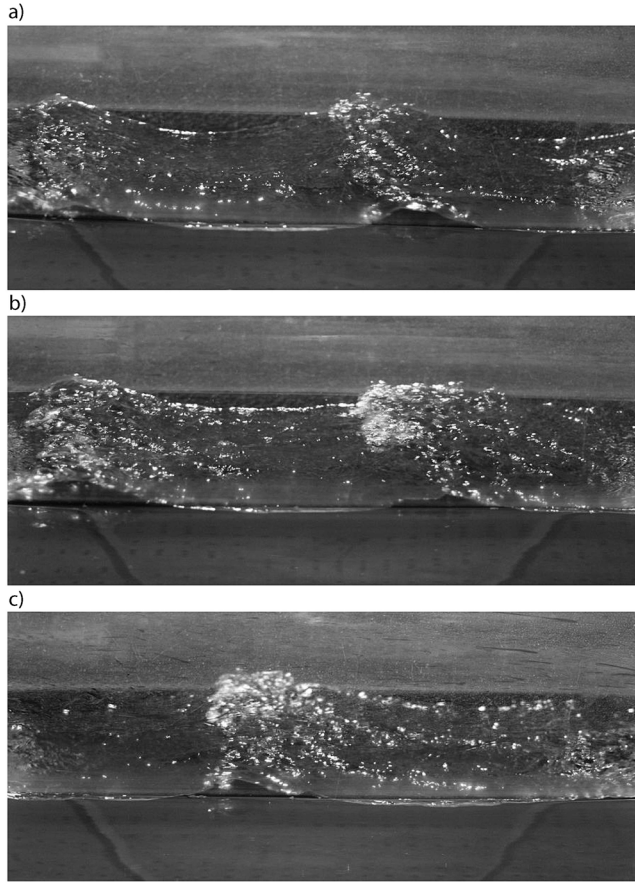


**Figure 8.** Examples of the wave images for different wind speeds  $U_{10}$ : (a)  $22 \text{ m s}^{-1}$ , (b)  $25 \text{ m s}^{-1}$ , and (c)  $27 \text{ m s}^{-1}$ . It is well seen that the intensive wave breaking with the foam on the crests starts from the wind speed  $25 \text{ m s}^{-1}$ .

392 smoothening of the waves, this leads to the saturation of  
393 the mean square slope of the wavefield. Basing on the the-  
394 oretical model of the wind turbulent boundary layer over  
395 wavy water surface, we investigated, whether this wind  
396 smoothening of the surface is sufficient for the explanation  
397 of the surface drag saturation or not.

### 398 3. The Theoretical Model of the Aerodynamic 399 Resistance of the Wavy Water Surface at Extreme 400 Wind Conditions

401 [36] An important part of the aerodynamic resistance of  
402 the water surface is the form drag. Then the first step in the  
403 theoretical interpretation of the effect of the sea surface drag  
404 reduction at strong winds is the calculation of the surface  
405 form drag. This part of the total aerodynamic resistance  
406 describes the influence of the roughness of the surface. It can  
407 be expected that the smoothening of the water surface by a  
408 very strong wind significantly reduces the form drag and can  
409 possibly explain the experimental results. The wind over  
410 waves is modeled as a turbulent boundary layer within the  
411 first-order semiempirical model of turbulence based on the  
412 Reynolds equations closed with the Boussinesq hypothesis

for turbulent stress with the self-similar eddy viscosity 413  
coefficient for the turbulent boundary layer 414

$$\nu = \nu_a f\left(\frac{u_* \eta}{\nu_a}\right), \quad (17)$$

where  $\nu_a$  is the air molecular viscosity. 415

[37] We used the approximation for  $f$  obtained by 416  
*Smolyakov* [1973] on the basis of the laboratory experiments 417  
on a turbulent boundary layer over the aerodynamically 418  
smooth plate 419

$$\nu = \nu_a \left\{ 1 + \kappa \frac{u_* \eta}{\nu_a} \left[ 1 - e^{-L \left( \frac{u_* \eta}{\nu_a} \right)^2} \right] \right\}. \quad (18)$$

[38] In this expression  $L$  is a number, which determines the 420  
scale of the viscous sublayer of a turbulent boundary layer; it 421  
depends on the regime of the flow over the surface. This 422  
comparison with the parameters of the velocity profile in the 423  
turbulent boundary layer from *Miles* [1959] gives  $L = 22.4$  424  
for the aerodynamically smooth surface,  $L = 13.3$  for the 425  
transition regime of a flow over surface, and  $L = 1.15$  for the 426  
rough surface. Turbulent viscosity can be specified as 427  
 $\nu_T = \nu - \nu_0$ . 428

[39] To verify the applicability of the model we compared 429  
the results of the calculation of the wind-wave growth rates 430  
within this model and the viscoelastic model of the turbu- 431  
lence similar to one suggested by *Miles* [1996]. Expressions 432  
for the eddy viscosity coefficient were derived from the set 433  
of equations for the turbulent Reynolds stresses described in 434  
*Rodi* [1980] 435

$$\frac{\partial \sigma_{ij}}{\partial t} + \langle u_k \rangle \frac{\partial \sigma_{ij}}{\partial x_k} = -C_1 \frac{\epsilon}{b} \left( \sigma_{ij} - \frac{2}{3} b \delta_{ij} \right) + \kappa b \left( \frac{\partial \langle u_i \rangle}{\partial x_j} + \frac{\partial \langle u_j \rangle}{\partial x_i} \right) - \frac{2}{3} \epsilon \delta_{ij}. \quad (19)$$

[40] Here  $b$  is the kinetic energy of turbulence,  $\epsilon$  is the rate of 436  
dissipation of the kinetic energy of turbulence,  $C_1 = 1.5-2.2$  is 437  
the empirical constant,  $b$  and  $\epsilon$  relate to the turbulent viscosity 438  
as follows:  $\nu_T \sim b^2/\epsilon$ . 439

[41] Linearizing (19), neglecting wave disturbances of  $b$  and 440  
 $\epsilon$  and taking into account the relationship of the kinetic energy 441  
of turbulence and the turbulent stresses in a turbulent boundary 442  
layer gives for the wave disturbances of turbulent stresses 443  
 $S_{ij} = \hat{S}_{ij} e^{-i(\omega t - kx)}$

$$S_{ij} = \nu_{wave} \left( \frac{\partial \langle u_i \rangle}{\partial x_j} + \frac{\partial \langle u_j \rangle}{\partial x_i} \right),$$

where 444

$$\nu_{wave} = \frac{\nu_T}{1 + \frac{\nu_T i (kU_0 - \omega) \alpha}{u_*^2}} \quad (20)$$

and  $\alpha$  is a constant of order 1. Obvious generalization of (20), 445  
which takes into account the turbulent transport in the viscous 446  
sublayer is as follows: 447

$$\nu_{wave} = \nu_0 + \frac{\nu - \nu_0}{1 + i \frac{(\nu - \nu_0)(kU_0 - \omega) \alpha}{u_*^2}}. \quad (21)$$



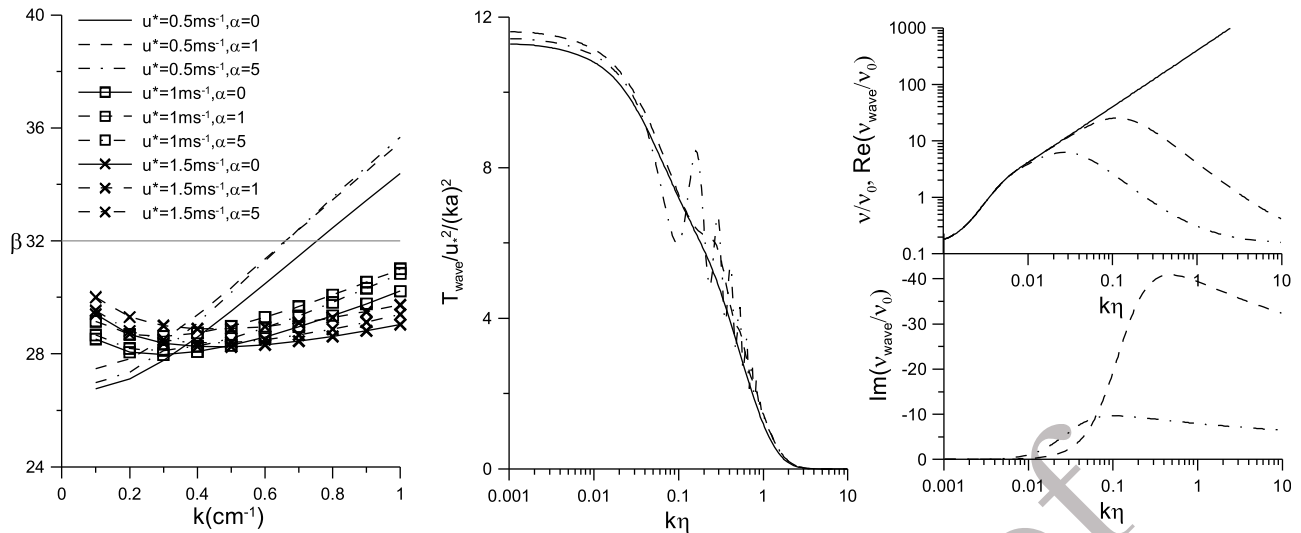


**Figure 9.** (left) Air-sea interaction parameter  $\beta$  via wave number calculated within the eddy viscosity model (19) and the model of viscoelastic turbulence (22), (middle) normalized profiles of the wave momentum flux (solid line, eddy viscosity model; dashed line, model of viscoelastic turbulence with  $\alpha = 1$ ; dash-dotted line,  $\alpha = 5$ ), and (right) profiles of the real and imaginary parts of effective viscosity coefficients.

448 [42] In Figure 9 (left) the dependencies of the wind-  
 449 wave interaction parameter  $\beta$  in the definition of *Belcher*  
 450 *et al.* [1994], which relates to the wind-wave growth rate  
 451 as follows:  $\text{Im}\omega = \frac{1}{2} \left(\frac{u_*}{c}\right)^2 \beta \omega$ , are presented for the parameters  
 452 of wind and waves typical for this experiment. It is visible,  
 453 that for the wave and wind parameters of these experiments  $\beta$   
 454 is not much sensitive to the model used in spite of the  
 455 noticeable drop of effective complex viscosity (see Figure 9,  
 456 right). It can be explained by Figure 9 (middle), where we  
 457 presented the scaled wave momentum flux, which is mostly  
 458 determined by the form drag of waves like the wind-wave  
 459 interaction parameter  $\beta$ . The quantities of  $\beta$  are closed to  
 460 the ones suggested by *Plant* [1982]:  $\beta_{\text{plant}} = 0.04 \pm 0.02$ ,  
 461  $\frac{\rho_a}{\rho_w} = 1.25 \cdot 10^{-3}$  and  $\beta = 32 \pm 16$ . Basing on this, we used  
 462 below a simpler model of eddy viscosity parameterization  
 463 for the further analysis.

464 [43] The wind-wave interaction is considered here in the  
 465 quasi-linear approximation similar to the approach devel-  
 466 oped by *Jenkins* [1992], *Janssen* [1989], and *Reutov and*  
 467 *Troitskaya* [1995]. Then disturbances induced in the airflow  
 468 by waves at the water surface are considered in the linear  
 469 approximation (see equations (A16a)–(A16c)) and the only  
 470 nonlinear effect taken into account is the wave momentum  
 471 flux caused by the demodulation of wave-induced dis-  
 472 turbances (see equation (A19)–(A21)). Let us discuss first  
 473 the applicability of the suggested model for the description  
 474 of the airflow over steep and breaking waves which occurred  
 475 in the flume at strong winds. The main features of the model  
 476 are as follows. It is based on the system of Reynolds equa-  
 477 tions with the first-order closing hypothesis. The wind-wave  
 478 interaction is considered within the quasi-linear approxi-  
 479 mation, i.e., wave-induced disturbances in the airflow are  
 480 considered in the linear approximation, but the resistive  
 481 effect of the wave momentum flux on the mean flow velocity

profile is taken into account, i.e., within the model the mean  
 airflow over waves is treated as nonseparated.

[44] One can expect the existence of strong nonlinear  
 phenomena such as sheltering, flow separation, etc., for the  
 cases of steep and breaking waves. The structure of an air-  
 flow over waves has been recently investigated in detail by  
 the method of Particle Image Velocimetry (PIV) [*Adrian*,  
 1991], when the flow is seeded with the small particles  
 illuminated by the laser light and then taken with a digital  
 camera. This technique was applied by *Reul et al.* [1999,  
 2008] and *Veron et al.* [2007] and clearly demonstrated the  
 effect of the airflow separation from the crests of the waves  
 and reattachment at the windward face of the wave on the  
 instantaneous patterns of the vector velocity fields.

[45] It should be emphasized that the PIV technique pro-  
 vides an instant picture of the velocity field, but the flow  
 separation in the turbulent boundary layer over a gravity  
 wave is a strongly nonstationary process due to both the  
 stochastic character of the airflow and the brevity of the  
 breaking event, which usually occurs within a small part of  
 the wave period [*Duncan et al.*, 1999]. At the same time, the  
 models of the air-sea fluxes and the wind-wave growth  
 exploit the wind flow parameters averaged over turbulent  
 fluctuations. We combined the measurements of the instant  
 airflow velocity fields over the surface waves with statistical  
 averaging [*Troitskaya et al.*, 2011]. The statistical ensemble  
 of such vector fields for subsequent averaging was obtained  
 by means of high-speed video filming and processing of the  
 video films by the PIV algorithm. Individual flow realiza-  
 tions manifested the typical features of flow separation  
 similar to those obtained by *Kawai* [1981, 1982], *Reul et al.*  
 [1999, 2008], and *Veron et al.* [2007]. The average para-  
 meters were retrieved by the phase averaging of the indi-  
 vidual vector fields. The averaged flow patterns appear  
 (кажутся, если надо сказать «оказываются», то turn out)

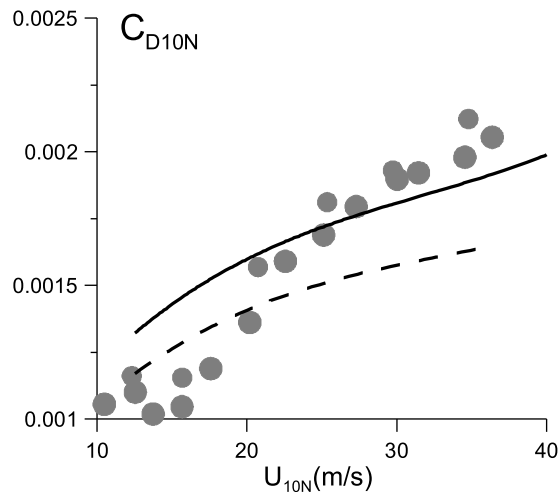


**Figure 10.** The dependence of the surface drag coefficient on the wind speed, comparing theory and the laboratory experiment. Circles, measurements; solid line, theoretical calculations with a short-wave spectrum of surface waves; dashed line, the neglected short-wave spectrum of surface waves.

517 to be smooth and slightly asymmetrical, with the minimum  
518 of the horizontal velocity near the water surface shifted to  
519 the leeward side of the wave profile.

520 [46] The results of these measurements were compared  
521 with the calculations within the quasi-linear model of the  
522 turbulent boundary layer described above. The wave para-  
523 meters (wavelength, celerity, steepness), used in this com-  
524 parison between the theory and the experiment, were  
525 retrieved from the same video films as those used for the  
526 airflow velocity calculations. The model calculations were in  
527 good agreement with the experimentally measured and  
528 conditionally averaged mean wind velocity, turbulent stress  
529 and also with the amplitude and phase of the main harmonics  
530 of the wave-induced velocity components [see *Troitskaya*  
531 *et al.*, 2011].

532 [47] Similarly, the applicability of the nonseparating  
533 quasi-linear theory for the description of average fields in the  
534 airflow over steep and even breaking waves, when the effect  
535 of separation is manifested at the instantaneous flow images  
536 was confirmed by DNS [Yang and Shen, 2010; Druzhinin  
537 *et al.*, 2012]. It can be qualitatively explained by strong  
538 intermittency of the flow separation observed in DNS. We  
539 were encouraged by these results to apply the quasi-linear  
540 model for the calculation of the form drag of the water sur-  
541 face at strong winds.

#### 542 4. Comparison of Theoretical Prediction 543 With Experimental Results: Discussion

544 [48] The form drag of the water surface was calculated  
545 within the model described above for the parameters (fric-  
546 tion velocity and wave spectra) measured in the flume. At  
547  $k < k_u$  the three-dimensional elevation spectrum  $S(\omega, k, \theta)$   
548 was taken from the experimental data. At  $k > k_u$  we used  
549 the approximation (16) with the *Elfouhaily et al.* [1997]  
550 spectrum (15). Special numerical tests showed, that the

calculated values of the aerodynamic resistance were only 551  
slightly sensitive to the frequency dependence of the spec- 552  
trum. Then in further calculations the real three-dimensional 553  
spectrum was replaced by the model one, in which the fre- 554  
quency dependence was taken as the delta function on the 555  
dispersion relation for free surface waves 556

$$S(\omega, k, \theta) = \delta(\omega - \omega(k)/2\pi)S(k, \theta).$$

[49] To investigate the sensitivity of the model to the spec- 557  
trum of surface waves we calculated  $C_D$ , when the contribu- 558  
tion of short surface waves was eliminated by a cutoff at the 559  
wave number  $1.2 \text{ cm}^{-1}$ . 560

[50] The obtained dependences of the drag coefficient on 561  
wind velocity are shown in Figure 10. It is clear that the 562  
model reproduces the tendency to saturation of the surface 563  
drag coefficient. Taking into account the short-wave part of 564  
the spectra yields quantitative agreement of the calculated 565  
and measured  $C_D$ . One of possible source of the differences 566  
between the calculated and measured dependences  $C_D(U_{10})$  567  
can be an inappropriate model of the high-frequency part of 568  
the wave spectra used in calculations, since the *Elfouhaily* 569  
*et al.* [1997] spectrum was adjusted for the sea, but not for 570  
lab conditions. Unfortunately, the measurement of the 571  
spectrum of short waves (cm and mm wavelength) with a 572  
high space resolution is a difficult problem especially at 573  
strong winds. The optical methods developed by *Jähne et al.* 574  
[2005] and *Rochoholz and Jähne* [2010] are promising for 575  
laboratory conditions. 576

#### 577 5. Conclusions

[51] The main objective of this work is the investigation of 578  
factors determining momentum exchange under high wind 579  
speeds basing on the laboratory experiment in a well-con- 580  
trolled environment. The experiments were carried out in the 581  
Thermo-Stratified Wind-Wave Tank (TSWIWAT) of the 582  
Institute of Applied Physics. The parameters of the facility 583  
are as follows: airflow  $0\text{--}25 \text{ m s}^{-1}$  (equivalent  $10 \text{ m}$  neutral 584  
wind speed  $U_{10}$  up to  $40 \text{ m s}^{-1}$ ), dimensions  $10 \text{ m} \times 0.4 \text{ m}$  585  
 $\times 0.7 \text{ m}$ , temperature stratification of the water layer. 586  
Simultaneous measurements of the airflow velocity profiles 587  
and wind waves were carried out in the wide range of wind 588  
velocities. Airflow velocity profile was measured by the 589  
scanning Pitot tube. The water elevation was measured by 590  
the three-channel wave gauge. Top and side views of the 591  
water surface were fixed by CCD camera. 592

[52] Wind friction velocity and the surface drag coeffi- 593  
cients were retrieved from the measurements by the profile 594  
method. The obtained values are in good agreement with the 595  
data of measurements by *Donelan et al.* [2004]. The direc- 596  
tional frequency-wave number spectra of the surface waves 597  
were retrieved by the algorithm similar to the wavelet 598  
directional method [Donelan *et al.*, 1996], but based on FFT. 599  
The obtained dependencies of the parameters of the wind 600  
waves indicate the existence of two regimes of the waves 601  
with the critical wind speed  $U_{cr}$  about  $25 \text{ m s}^{-1}$ . For  $U_{10} >$  602  
 $U_{cr}$  the mean square slope of wind waves demonstrated 603  
some tendency to saturation. The surface drag also tends to 604  
saturation for  $U_{10} > U_{cr}$  similarly to *Donelan et al.* [2004]. 605  
Video filming indicates the onset of wave breaking with the 606

607 white capping and spray generation at wind speeds approx-  
608 imately equal to  $U_{cr}$ . Based on the experimental data, a  
609 possible physical mechanism of the drag is suggested.  
610 Tearing of the wave crests at severe wind conditions leads to  
611 the effective smoothing (decreasing wave slopes) of the  
612 water surface, which in turn reduces the aerodynamic  
613 roughness of the water surface.

614 [53] We compared the obtained experimental dependen-  
615 cies with the predictions of the quasi-linear model of the  
616 turbulent boundary layer over the waded water surface  
617 [Reutov and Troitskaya, 1995]. The comparison shows that  
618 the theoretical predictions give low estimates for the mea-  
619 sured drag coefficient and wavefields. Taking into account  
620 momentum flux, associated with the high-frequency part of  
621 the wind-wave spectra, yields theoretical estimations in good  
622 agreement with the experimental data.

## 623 Appendix A

624 [54] The wind flow is described within the first-order  
625 semiempirical model of turbulence based on the set of the  
626 Reynolds equations

$$\frac{\partial \langle u_i \rangle}{\partial t} + \langle u_j \rangle \frac{\partial \langle u_i \rangle}{\partial x_j} + \frac{1}{\rho_a} \frac{\partial \langle p \rangle}{\partial x_i} = \frac{\partial \sigma_{ij}}{\partial x_j} \quad (A1)$$

627 and the following expressions for the tensor of turbulence  
628 stresses:

$$\sigma_{ij} = \nu u'_i u'_j = \nu \left( \frac{\partial \langle u_i \rangle}{\partial x_j} + \frac{\partial \langle u_j \rangle}{\partial x_i} \right). \quad (A2)$$

628 [55] Here  $\langle \dots \rangle$  denotes the quantities averaged over tur-  
629 bulent fluctuations,  $\nu$  is the turbulent viscosity coefficient, a  
630 given function of  $z$ . We use a self-similar expression for the  
631 eddy viscosity coefficient in the turbulent boundary layer  
632 expressed by equation (19).

633 [56] The boundary conditions at the air-sea interface  
634  $z = \xi(x, y, t)$  are

$$\frac{\partial \xi}{\partial t} + \langle u \rangle \frac{\partial \xi}{\partial x} + \langle v \rangle \frac{\partial \xi}{\partial y} \Big|_{z=\xi(x,y,t)} = \langle w \rangle \Big|_{z=\xi(x,y,t)}, \quad (A3)$$

$$\langle \vec{u}_\tau^w \rangle \Big|_{z=\xi(x,y,t)} = \langle \vec{u}_\tau^a \rangle \Big|_{z=\xi(x,y,t)}, \quad (A4)$$

635  $\langle u \rangle$ ,  $\langle v \rangle$  are the  $x$  and  $y$  components of the velocity field in  
636 the air, averaged over turbulent fluctuations,  $\langle \vec{u}_\tau^w \rangle = \langle \vec{u}_\tau^a \rangle$   
637 are the tangential velocity components in water and in air,  
638  $\langle w \rangle$  is the  $z$  component of the velocity field in the air.

639 [57] The random field of the water surface elevation is  
640 presented as a Fourier-Stieltjes transform

$$\xi(\vec{r}, t) = \int dA(\vec{k}, \omega) e^{i(\vec{k}\vec{r} - \omega t)}, \quad (A5)$$

641 here  $\vec{k} = (k_x, k_y)$  is a two-dimensional wave vector,  $\omega$  is the  
642 frequency of surface waves.

[58] For a statistically homogeneous and stationary pro- 643  
cess the wave number-frequency spectrum  $F(\vec{k}, \omega)$  can be 644  
introduced as follows: 645

$$\langle dA(\vec{k}, \omega) dA(\vec{k}_1, \omega_1) \rangle = F(\vec{k}, \omega) \delta(\vec{k} - \vec{k}_1) \delta(\omega - \omega_1) d\vec{k} d\vec{k}_1 d\omega d\omega_1. \quad (A6)$$

[59] To avoid strong geometric nonlinearity, the transfor- 646  
mation to the wave-following curvilinear coordinates is 647  
performed

$$\begin{aligned} x &= \zeta_1 + \int i \cos\vartheta e^{i(k(\zeta_1 \cos\vartheta + \zeta_2 \sin\vartheta) - \omega t) - k\eta - i\varphi} dA, \\ y &= \zeta_2 + \int i \sin\vartheta e^{i(k(\zeta_1 \cos\vartheta + \zeta_2 \sin\vartheta) - \omega t) - i\varphi - k\eta} dA, \\ z &= \eta + \int e^{i(k(\zeta_1 \cos\vartheta + \zeta_2 \sin\vartheta) - \omega t) - i\varphi - k\eta} dA, \end{aligned} \quad (A7)$$

here  $\theta$  is the angle between the wave number wave vector  $\vec{k}$  648  
and direction of  $x$  axis. In the linear approximation the coor- 649  
dinate surface  $\eta = 0$  coincides with the waded water surface. 650

[60] The solution to the set of the Reynolds equations (A1) 651  
is searched as a superposition of mean wind field  $\vec{U}_0(\eta)$  and 652  
the disturbances induced in the airflow by the waves at the 653  
water surface. Then, the velocity field is as follows: 654

$$\langle \vec{u} \rangle = \vec{U}_0(\eta) + \int \vec{u}'(\eta) e^{i(k(\zeta_1 \cos\vartheta + \zeta_2 \sin\vartheta) - \omega t) - i\varphi - k\eta} k dA. \quad (A8)$$

[61] The wind-wave interaction is considered here in the 655  
quasi-linear approximation similar to the approach developed 656  
by Jenkins [1992], Janssen [1989], and Reutov and 657  
Troitskaya [1995]. Then the wave disturbances induced in 658  
the airflow by the waves at the water surface are described in 659  
the linear approximation and can be considered indepen- 660  
dently. The coordinate transformation (A7) can be consid- 661  
ered as a superposition of formal coordinate transformations 662  
for each single harmonic. Nonlinear terms or wave momen- 663  
tum fluxes enter into the equations for the components of 664  
mean velocity. 665

[62] Considering first equations for the disturbances, induced 666  
by a single harmonic wave at the water surface with the wave 667  
vector  $\vec{k}$ , frequency  $\omega$  and amplitude  $dA$ , we introduce the 668  
formal coordinate transformation, where the coordinate line  $\eta =$  669  
0 coincides with the water surface disturbed by this single 670  
harmonic wave 671

$$\begin{aligned} x &= \zeta_1 + i \cos\vartheta e^{i(k(\zeta_1 \cos\vartheta + \zeta_2 \sin\vartheta) - \omega t) - k\eta - i\varphi} dA, \\ y &= \zeta_2 + i \sin\vartheta e^{i(k(\zeta_1 \cos\vartheta + \zeta_2 \sin\vartheta) - \omega t) - k\eta - i\varphi} dA, \\ z &= \eta + e^{i(k(\zeta_1 \cos\vartheta + \zeta_2 \sin\vartheta) - \omega t) - i\varphi - k\eta} dA. \end{aligned} \quad (A9)$$

[63] The linear coordinate transformation 672

$$\begin{aligned} \zeta'_1 &= \zeta_1 \cos\vartheta + \zeta_2 \sin\vartheta - \frac{\omega}{k} t, \\ \zeta'_2 &= \zeta_2 \cos\vartheta - \zeta_1 \sin\vartheta = y_2 \cos\vartheta - y_1 \sin\vartheta = y', \end{aligned} \quad (A10)$$

defines the reference frame following this harmonic wave, 673  
where the wavefield does not depend on  $\zeta'_2$  (or Cartesian 674

675 coordinate  $y'$ , i.e., it depends only on two coordinates  $\zeta'_1$   
676 and  $\eta$ . Tangential velocity components are transformed  
677 similar to (A10), and in the new reference frame

$$\begin{aligned} u' &= u \cos\vartheta + v \sin\vartheta - \frac{\omega}{k}, \\ v' &= -u \sin\vartheta + v \cos\vartheta. \end{aligned} \quad (\text{A11})$$

678 [64] It means that the stream function  $\Phi$  can be introduced  
679 for the motions in the plane  $\zeta'_2 = y' = \text{const}$  as follows:

$$u' = \frac{\partial\Phi}{\partial\eta}, \quad w' = -\frac{\partial\Phi}{\partial\zeta'_1} \quad (\text{A12})$$

680 and the Reynolds equations can be formulated in terms of  
681 stream function  $\Phi$  and vorticity  $\chi$

$$\begin{aligned} \frac{\partial\chi}{\partial t} + \frac{1}{I} \frac{\partial\chi}{\partial\zeta'_1} \left( \frac{\partial\Phi}{\partial\eta} \right) - \frac{1}{I} \frac{\partial\chi}{\partial\eta} \left( \frac{\partial\Phi}{\partial\zeta'_1} \right) \\ = \Delta(\nu\chi) - \frac{2}{I^2} \nu_{\eta\eta} \frac{\partial^2\Phi}{\partial\zeta'^2_1} - \frac{I_\eta}{I^3} \left( (\Phi_\eta \nu_\eta)_\eta - \nu_\eta \Phi_{\zeta'_1\zeta'_1} \right) \\ - \frac{I_{\zeta'_1}}{I^3} (2\nu_\eta \Phi_{\zeta'_1\eta} - \Phi_{\zeta'_1} \nu_{\eta\eta}) + \Phi_\eta \nu_\eta \frac{I^2_{\zeta'_1} + I^2_\eta}{I^4}, \end{aligned} \quad (\text{A13a})$$

$$\Delta\Phi = \chi = \frac{1}{I} (\Phi_{\zeta'_1\zeta'_1} + \Phi_{\eta\eta}) \quad (\text{A13b})$$

682 here  $I$  is the Jacobian of transformation (A9). The transversal  
683 velocity component  $v'$  does not enter the equations (A13a)  
684 and (A13b), and  $v'$  obeys the following equation:

$$\frac{\partial v'}{\partial t} + \frac{1}{I} \left( \frac{\partial v'}{\partial\zeta'_1} \frac{\partial\Phi}{\partial\eta} - \frac{\partial v'}{\partial\eta} \frac{\partial\Phi}{\partial\zeta'_1} \right) = \Delta(v'\nu) + \frac{1}{I} v' \nu_{\eta\eta}. \quad (\text{A14})$$

685 [65] We search the solution to the system (A13a)–(A14) as  
686 a superposition of the mean field and harmonic wave dis-  
turbance

$$\begin{aligned} \Phi &= \int \left( U_0(\eta) \cos\vartheta + V_0(\eta) \sin\vartheta - \frac{\omega}{k} \right) d\eta + \Phi_1(\eta) dA e^{ik\zeta'_1}, \\ v &= V_0(\eta) \cos\vartheta - U_0(\eta) \sin\vartheta + V_1(\eta) dA e^{ik\zeta'_1}, \end{aligned} \quad (\text{A15a})$$

$$\chi = U_{0\eta} \cos\vartheta + V_{0\eta} \sin\vartheta + X_1(\eta) dA e^{ik\zeta'_1}. \quad (\text{A15b})$$

687 [66] Equations for complex amplitudes  $\Phi_1(\eta)$ ,  $\chi_1(\eta)$ ,  $V_1(\eta)$   
688 are obtained by the linearization of the system (A13a)–(A14)

$$\begin{aligned} (\Phi_{0\eta} X_1 - \Phi_1 \chi_{0\eta}) ik - \left( \frac{d^2}{d\eta^2} - k^2 \right) (X_1 \nu) \\ = -2\nu_\eta \Phi_1 k^2 - 2kA e^{-k\eta} (\Phi_{0\eta} \nu_\eta)_\eta, \end{aligned} \quad (\text{A16a})$$

$$\frac{d^2\Phi_1}{d\eta^2} - k^2\Phi_1 = X_1 - 2k e^{-k\eta} \Phi_{0\eta\eta}, \quad (\text{A16b})$$

$$(\Phi_{0\eta} V_1 - \Phi_1 V_\eta) ik = \nu \left( \frac{d^2}{d\eta^2} - k^2 \right) V_1 + \nu_\eta V_{1\eta} k^2. \quad (\text{A16c})$$

[67] We consider the solutions to the system (A15a)–(A16) 689  
decreasing at large distances from the surface, i.e., 690

$$\Phi_1|_{\eta \rightarrow \infty} \rightarrow 0; \quad V_1|_{\eta \rightarrow \infty} \rightarrow 0. \quad (\text{A17})$$

[68] The boundary conditions at the water surface for the 691  
system (A16) follow from (A4) and (A5) are expressed in 692  
curvilinear coordinates [see *Reutov and Troitskaya*, 1995] for 693  
details

$$\Phi_1|_{\eta=0} = 0; \quad \Phi_{1\eta}|_{\eta=0} = 2\omega; \quad V_1|_{\eta=0} = 0. \quad (\text{A18})$$

[69] The only nonlinear effect taken into account in the 694  
quasi-linear approximation is the demodulation of the wave 695  
disturbances induced in the airflow by waves at the water 696  
surface. Equations for mean velocity profile components 697  
 $U_0(\eta)$  and  $V_0(\eta)$  are obtained by the following steps. Aver- 698  
aging (A13a) and (A13b) over  $\zeta'_1$  gives the equation for  $\Phi_0$  699  
and averaging (A14) yields the equation for  $\nu_0(\eta)$ . Express- 700  
ing  $U_0(\eta)$  and  $V_0(\eta)$  via  $\Phi_0(\eta)$  and  $\nu_0(\eta)$  by inversion (A15a) 701  
and (A15b) and integrating over the wind-wave spectrum 702  
gives

$$\begin{aligned} \frac{d}{d\eta} \left( \nu \frac{d(U_0, V_0)}{d\eta} \right) &= \int \left( \tau_{\parallel}(\eta, k, \varphi, \omega)(\eta) \begin{pmatrix} \cos\varphi \\ \sin\varphi \end{pmatrix} \right. \\ &\quad \left. + \tau_{\perp}(\eta, k, \varphi, \omega)(\eta) \begin{pmatrix} -\sin\varphi \\ \cos\varphi \end{pmatrix} \right) \\ &\quad \cdot k^2 F(k, \varphi, \omega) k dk d\varphi d\omega, \end{aligned} \quad (\text{A19})$$

here  $\tau_{\parallel}(\eta, k, \theta, \omega)(\eta)$ ,  $\tau_{\perp}(\eta, k, \theta, \omega)(\eta)$  are the components of 703  
the wave momentum flux induced by the surface wave with 704  
the wave number  $k$ , frequency  $\omega$  propagating at the angle  $\theta$  705  
to the wind. 706

[70] The expression for  $\tau_{\parallel}(\eta, k, \theta, \omega)(\eta)$  follows from 707  
(A13a) and (A13b) 708

$$\tau_{\parallel}(\eta, k, \varphi, \omega)(\eta) = k [k\nu_\eta \text{Re}(\Phi_{1\eta} - k\Phi_1) e^{-k\eta} + 2k^2 e^{-2k\eta} \nu_\eta U_0 \cos\varphi] \quad (\text{A20})$$

and the expression for  $\tau_{\perp}(\eta, k, \theta, \omega)(\eta)$  follows from (A14): 709

$$\tau_{\perp}(\eta, k, \omega) = -\frac{1}{2} k \frac{d}{d\eta} \text{Im}(\Phi_1^* V_1). \quad (\text{A21})$$

[71] Equations (A19) express the conservation law for the 710  
vertical flux of two projections of the horizontal momentum 711  
component in the turbulent boundary layer. If the turbulent 712  
shear stress at a large distance from the surface is directed 713  
along  $x$ , the conservation law for the mean momentum 714  
components may be written as follows: 715

$$\tau_{turb}^{(x)}(\eta) + \tau_{\parallel}(\eta) = u_*^2 \quad (\text{A22})$$

$$\tau_{turb}^{(y)}(\eta) + \tau_{\perp}(\eta) = 0. \quad (\text{A23})$$

[72] **Acknowledgments.** We are grateful to S. S. Zilitinkevich, G. G. 716  
Golytsyn, and V. N. Kudryavtsev for fruitful discussion and constructive 717  
criticism. This work was supported by a grant from the Government of 718  
the Russia Federation designed to support scientific research projects imple- 719  
mented under the supervision of leading scientists at Russian institutions of 720

- 721 higher learning (project code 11.G34.31.0048); grants RFBR 10-05-00339,  
722 09-05-00779, and 11-08-97067; FTP scientific and scientific pedagogical  
723 caded of 343 innovative Russia and FTP investigations in priority-driven  
724 directions of the modernization of Russian scientific technology complex;  
725 and President grant for young scientists MK-5575.2012.5.
- 726 **References**
- 727 Adrian, R. J. (1991), Particle imaging techniques for experimental fluid  
728 mechanics, *Annu. Rev. Fluid Mech.*, *23*, 261–304, doi:10.1146/annurev.  
729 fl.23.010191.001401.
- 730 Andreas, E. L. (2004), Spray stress revised, *J. Phys. Oceanogr.*, *34*(6),  
731 1429–1440, doi:10.1175/1520-0485(2004)034<1429:SSR>2.0.CO;2.
- 732 Andreas, E. L., and K. A. Emanuel (2001), Effects of sea spray on tropical  
733 cyclone intensity, *J. Atmos. Sci.*, *58*(24), 3741–3751, doi:10.1175/1520-  
734 0469(2001)058<3741:EOSSOT>2.0.CO;2.
- 735 Barenblatt, G. I., and G. S. Golitsyn (1974), Local structure of mature dust  
736 storms, *J. Atmos. Sci.*, *31*(7), 1917–1933, doi:10.1175/1520-0469(1974)  
737 031<1917:LSOMDS>2.0.CO;2.
- 738 Belcher, S. E., J. A. Harris, and R. L. Street (1994), Linear dynamics of  
739 wind waves in coupled turbulent air-water flow. Part 1. Theory, *J. Fluid*  
740 *Mech.*, *271*, 119–151, doi:10.1017/S0022112094001710.
- 741 Donelan, M. A., B. K. Haus, N. Reul, W. J. Plant, M. Stiassnie, H. C. Graber,  
742 O. B. Brown, and E. S. Saltzman (2004), On the limiting aerodynamic  
743 roughness of the ocean in very strong winds, *Geophys. Res. Lett.*, *31*,  
744 L18306, doi:10.1029/2004GL019460.
- 745 Druzhinin, O. A., Y. I. Troitskaya, and S. S. Zilitinkevich (2012), Direct  
746 numerical simulation of a turbulent wind over 21 a wavy water surface,  
747 *J. Geophys. Res.*, *117*, C00J05, doi:10.1029/2011JC007789.
- 748 Duncan, J. H., H. Qiao, V. Philomin, and A. Wenz (1999), Gentle spilling  
749 breakers: Crest profile evolution, *J. Fluid Mech.*, *379*, 191–222,  
750 doi:10.1017/S0022112098003152.
- 751 Elfouhaily, T. B., B. Chapron, K. Katsaros, and D. Vandemark (1997), A uni-  
752 fied directional spectrum for long and short wind-driven waves, *J. Geophys.*  
753 *Res.*, *107*, 15,781–15,796, doi:10.1029/97JC00467.
- 754 Emanuel, K. A. (1995), Sensitivity of tropical cyclones to surface  
755 exchange coefficients and a revised steady-state model incorporating  
756 eye dynamics, *J. Atmos. Sci.*, *52*(22), 3969–3976, doi:10.1175/1520-  
757 0469(1995)052<3969:SOTCTS>2.0.CO;2.
- 758 Emanuel, K. (2003), Tropical cyclones, *Annu. Rev. Earth Planet. Sci.*, *31*,  
759 75–104, doi:10.1146/annurev.earth.31.100901.141259.
- 760 Fairall, C. W., E. F. Bradley, J. E. Hare, A. A. Grachev, and J. B. Edson  
761 (2003), Bulk parameterization of air-sea fluxes: Updates and verification  
762 for the COARE algorithm, *J. Clim.*, *16*(4), 571–591, doi:10.1175/1520-  
763 0442(2003)016<0571:BPOASF>2.0.CO;2.
- 764 Hara, T., and S. E. Belcher (2004), Wind profile and drag coefficient  
765 over mature ocean surface wave spectra, *J. Phys. Oceanogr.*, *34*(11),  
766 2345–2358, doi:10.1175/JPO2633.1.
- 767 Hinze, J. O. (1959), *Turbulence: An Introduction to Its Mechanism and*  
768 *Theory*, 586 pp., McGraw-Hill, New York.
- 769 Hsu, C. T., and E. Y. Hsu (1983), On the structure of turbulent flow over a  
770 progressive water wave: Theory and experiment in a transformed wave-  
771 following coordinate system. Part 2, *J. Fluid Mech.*, *131*, 123–153,  
772 doi:10.1017/S0022112083001263.
- 773 Hsu, C. T., E. Y. Hsu, and R. L. Street (1981), On the structure of turbulent  
774 flow over a progressive water wave: Theory and experiment in a trans-  
775 formed, wave-following co-ordinate system, *J. Fluid Mech.*, *105*, 87–  
776 117, doi:10.1017/S0022112081003121.
- 777 Jähne, B., M. Schmidt, and R. Rocholz (2005), Combined optical slope/  
778 height measurements of short wind waves: Principles and calibration,  
779 *Meas. Sci. Technol.*, *16*, 1937–1944, doi:10.1088/0957-0233/16/10/008.
- 780 Janssen, P. A. E. M. (1989), Wave-induced stress and the drag of air flow  
781 over sea waves, *J. Phys. Oceanogr.*, *19*(6), 745–754.
- 782 Janssen, P. A. E. M. (1991), Quasi-linear theory of wind wave generation  
783 applied to wave forecasting, *J. Phys. Oceanogr.*, *21*(11), 1631–1642,  
784 doi:10.1175/1520-0485(1991)021<1631:QLTOWW>2.0.CO;2.
- 785 Jarosz, E., D. A. Mitchell, D. W. Wang, and W. J. Teague (2007) Bottom-  
786 up determination of air-sea momentum exchange under a major tropical  
787 cyclone, *Science*, *315*, 1707–1709, doi:10.1126/science.1136466.
- 788 Jenkins, A. D. (1992), Quasi-linear eddy-viscosity model for the flux of  
789 energy and momentum to wind waves using conservation-law equations  
in a curvilinear coordinate system, *J. Phys. Oceanogr.*, *22*(8), 843–858,  
doi:10.1175/1520-0485(1992)022<0843:AQLEVM>2.0.CO;2.
- Kawai, S. (1981), Visualization of air flow separation over wind wave crest  
under moderate wind, *Boundary Layer Meteorol.*, *21*, 93–104,  
doi:10.1007/BF00119370.
- Kawai, S. (1982), Structure of air flow separation over wind wave crest,  
*Boundary Layer Meteorol.*, *23*, 503–521, doi:10.1007/BF00116275.
- Kudryavtsev, V., and V. Makin (2007), Aerodynamic roughness of the sea  
surface at high winds, *Boundary Layer Meteorol.*, *125*, 289–303,  
doi:10.1007/s10546-007-9184-7.
- Kudryavtsev, V., and V. Makin (2011), Impact of ocean spray on the dynam-  
ics of the marine atmospheric boundary layer, *Boundary Layer Meteorol.*,  
*140*, 383–410, doi:10.1007/s10546-011-9624-2.
- Kukulka, T., T. Hara, and S. E. Belcher (2007), A model of the air-sea  
momentum flux and breaking-wave distribution for strongly forced wind  
waves, *J. Phys. Oceanogr.*, *37*(7), 1811–1828, doi:10.1175/JPO3084.1.
- Large, W. G., and S. Pond (1981), Open ocean momentum flux measure-  
ments in moderate to strong winds, *J. Phys. Oceanogr.*, *11*(3), 324–336,  
doi:10.1175/1520-0485(1981)011<0324:OOMFMI>2.0.CO;2.
- Makin, V. K., V. N. Kudryavtsev, and C. Mastenbroek (1995), Drag of the  
sea surface, *Boundary Layer Meteorol.*, *73*, 159–182, doi:10.1007/  
BF00708935.
- Mastenbroek, C., V. K. Makin, M. H. Garat, and J. P. Giovanangeli (1996),  
Experimental evidence of the rapid distortion of turbulence in the air flow  
over water waves, *J. Fluid Mech.*, *318*, 273–302, doi:10.1017/  
S0022112096007124.
- Miles, J. W. (1959), On the generation of surface waves by shear flows. Part  
2, *J. Fluid Mech.*, *6*, 568–582, doi:10.1017/S0022112059000830.
- Miles, J. (1996), Surface-wave generation: A visco-elastic model, *J. Fluid*  
*Mech.*, *322*, 131–145, doi:10.1017/S002211209600273X.
- Powell, M. D. (2007), Drag coefficient distribution and wind speed depen-  
dence in tropical cyclones, final report, Atl. Oceanogr. and Meteorol.  
Lab., Natl. Oceanic and Atmos. Admin., Key Biscayne, Fla.
- Powell, M. D., P. J. Vickery, and T. A. Reinhold (2003), Reduced drag coef-  
ficient for high wind speeds in tropical cyclones, *Nature*, *422*, 279–283,  
doi:10.1038/nature01481.
- Reul, N., H. Branger, and G. P. Giovanangeli (1999), Air flow separation  
over unsteady breaking waves, *Phys. Fluids*, *11*(7), 1959–1961,  
doi:10.1063/1.870058.
- Reul, N., H. Branger, and J.-P. Giovanangeli (2008), Air flow structure over  
short-gravity breaking water waves, *Boundary Layer Meteorol.*, *126*,  
477–505, doi:10.1007/s10546-007-9240-3.
- Reutov, V. P., and Y. I. Troitskaya (1995), On the nonlinear effects in the  
interaction of gravity waves with turbulent airflow, *Izv. Russ. Acad. Sci.*  
*Atmos. Oceanic Phys.*, *31*(6), 825–834.
- Rocholz, R., and B. Jähne (2010), Spatio-temporal measurements of short  
wind water waves, *Geophys. Res. Abstr.*, *12*, EGU2010-5509.
- Rodi, W. (1980), Models for environmental turbulence, in *Prediction Methods*  
*for Turbulent Flows*, edited by W. Kollmann, pp. 227–322, Hemisphere  
Publ., Washington, D. C.
- Smolyakov, A. V. (1973), Spectrum of the quadruple radiation of the plane  
turbulent boundary layer, *Acoust. Phys.*, *19*(3), 420–425.
- Taylor, P. K., and M. J. Yelland (2001), The dependence of sea surface  
roughness on the height and steepness of the waves, *J. Phys. Oceanogr.*,  
*31*(2), 572–590.
- Troitskaya, Y. I., and G. V. Rybushkina (2008), Quasi-linear model of  
interaction of surface waves with strong and hurricane winds, *Izv. Russ.*  
*Acad. Sci. Atmos. Oceanic Phys.*, *44*(5), 621–645, doi:10.1134/  
S0001433808050083.
- Troitskaya, Y., D. Sergeev, O. Ermakova, and G. Balandina (2011), Statisti-  
cal parameters of the air turbulent boundary layer over steep water waves  
measured by the PIV technique, *J. Phys. Oceanogr.*, *41*, 1421–1454,  
doi:10.1175/2011JPO4392.1.
- Veron, F., G. Saxena, and S. K. Misra (2007), Measurements of the viscous  
tangential stress in the airflow above wind waves, *Geophys. Res. Lett.*, *34*,  
L19603, doi:10.1029/2007GL031242.
- Yang, D., and L. Shen (2010), Direct-simulation-based study of turbulent  
flow over various wavy boundaries, *J. Fluid Mech.*, *650*, 131–180,  
doi:10.1017/S0022112009993557.
- Young, I. R. (2003), A review of the sea state generated by hurricanes, *Mar.*  
*Struct.*, *16*, 201–218, doi:10.1016/S0951-8339(02)00054-0.